POLITECNICO DI TORINO
Repository ISTITUZIONALE

Metal-to-ceramic joining for high-temperature Na-Zn batteries

Original
Metal-to-ceramic joining for high-temperature Na-Zn batteries / D'Isanto, F., Baggio, A., Salvo, M., Smeacetto, F.. - In: CERAMICS INTERNATIONAL. - ISSN 0272-8842. - 52:13(2026), pp. 22121-22132. [10.1016/j.ceramint.2026.03.279]

Availability:
This version is available at: 11583/3012647 since: 2026-07-02T16:21:54Z

Publisher:
ELSEVIER SCI LTD

Published
DOI:10.1016/j.ceramint.2026.03.279

Terms of use:

This article is made available under terms and conditions as specified in the corresponding bibliographic description in the repository

Publisher copyright

(Article begins on next page)

21 November 2026

Ceramics International 52 (2026) 22121–22132

Contents lists available at ScienceDirect

Ceramics International

journal homepage: www.elsevier.com/locate/ceramint

Metal-to-ceramic joining for high-temperature Na-Zn batteries

F. D'Isanto *, A. Baggio, M. Salvo, F. Smeacetto

Politecnico di Torino, Department of Applied Science and Technology (DISAT), Corso Duca degli Abruzzi 24, 10129, Torino, Italy

ARTICLE INFO

Keywords:
Invar42 alloy
Metal-ceramic joining
Glass-based sealants
Liquid metal batteries
Na-Zn molten-salt batteries

ABSTRACT

Reliable metal-to-ceramic joining is crucial for the development of high-temperature Na–Zn batteries. This work investigates the joining of Invar42 (Fe–Ni alloy) to alumina using two glass-based composite sealants: a commercial silica-containing glass (SG) and a newly developed silica-free Y_2O_3–Al_2O_3–B_2O_3–BaO composition (YABB), both modified with 25 wt% Al_2O_3. In situ high-temperature XRD was used to examine the pre-oxidation behaviour of Invar42 at 650–750 °C. Pre-oxidation at 700 °C produced a uniform oxide layer approximately 5 μm thick, which was selected as the oxide scale to enhance wetting and adhesion between Invar42 and the glass sealant. Among the tested sealants, SG-25A (SG + 25 wt% Al_2O_3) showed the best thermo-mechanical compatibility, resulting in crack-free joined samples that remained stable after 150 h at 600 °C and during thermal cycling. Mechanical tests yielded an average apparent shear strength of 23 ± 7 MPa, with failure occurring predominantly within the oxide scale.

1. Introduction

Renewable intermittent energy sources, such as solar and wind power, play a crucial role in the transition toward a low-carbon energy sector. To effectively balance production and consumption, energy storage systems are essential, serving both grid stabilisation and load-levelling functions. These storage solutions should be cost-effective and based on abundant, readily accessible materials [1]. One promising candidate could be a liquid molten-salt Na-Zn battery, which operates at high temperatures in the range of 400-600 °C. Due to its high operating temperature, volume, and weight, this type of battery is not suitable for mobile applications. However, for stationary energy storage requiring large capacities at minimal cost, liquid sodium batteries offer significant potential [2]. The stability of selected materials in the presence of liquid or vapor sodium is therefore critical; consequently, the design and study of both structural and joining materials, represent a significant challenge [3].

Alumina has been recognised as one of the most suitable candidates for insulating components in terms of sodium reactivity due to its high-temperature stability, electrical insulation, low electron conductivity, and, most importantly, high resistance to Na corrosion, at least up to 800 °C [4–8]. Furthermore, owing to its high availability and relatively low cost compared with alternative materials, alumina represents an optimal insulator for a liquid-metal battery design [9].

In many cases, alumina is used in combination with metallic components [10–13] to provide mechanical strength and rigidity in applications such as battery casings. This makes the study of metal–ceramic joints particularly relevant. The development of reliable metal-to-ceramic bonds is particularly challenging due to differences in the coefficients of thermal expansion (CTEs) of the joined materials, which can lead to residual stresses and cracking during cooling, as well as to the inherently poor wetting of most metals on ceramic surfaces. In the past, several solutions have been investigated, such as welding, diffusion bonding, and brazing[10,14–16]. One of the most effective solutions is the use of glass and glass-ceramic materials as joining media, due to their compositional versatility, which enables precise tailoring of properties to meet specific application requirements [17]. Key parameters such as the coefficient of thermal expansion (CTE), glass transition temperature (T_g), chemical reactivity, and mechanical strength can be finely tuned to optimise performance. Additionally, these materials are renowned for their exceptional thermal stability at high temperatures and in harsh environments [18,19], as well as for their high chemical resistance [20,21], properties that render them particularly advantageous for applications in the aerospace, nuclear, and energy sectors [21–26].

In sodium-based battery applications, various sealing materials have been investigated. Smeacetto et al. [27] developed a boroaluminosilicate glass-ceramic demonstrating excellent resistance to molten sodium at 300 °C for up to 10 h and stability under operating conditions between 250 and 320 °C for 250 h. However, the silica

* Corresponding author.
E-mail address: fabiana.disanto@polito.it (F. D'Isanto).

https://doi.org/10.1016/j.ceramint.2026.03.279
Received 3 February 2026; Received in revised form 12 March 2026; Accepted 18 March 2026
Available online 20 March 2026
0272-8842/© 2026 The Authors. Published by Elsevier Ltd. This is an open access article under the CC BY-NC-ND license (http://creativecommons.org/licenses/by-nc-nd/4.0/).

content significantly influences corrosion resistance in alkali environments. Park et al. [28] observed a decrease in chemical durability with increasing SiO_2 content. To address this issue, they subsequently developed a patented low-silica glass composition (8–10 wt%) with enhanced chemical stability against sodium corrosion, suitable for metal-to-ceramic joints with Kovar or molybdenum [29]. Further studies confirmed that silica-free glasses exhibit improved chemical stability. Manthina et al. [30] investigated an alkaline-earth aluminoborate glass and found that higher Bi_2O_3 contents reduced sodium corrosion resistance. Burggraaf et al. [31] evaluated aluminoborate glasses in sodium vapor at 500–850 °C for up to 48 h, reporting that high B_2O_3 content could compromise stability and increase thermal expansion above T_g. Kumar et al. [32] patented a silica-free glass containing B_2O_3, Al_2O_3, BaO, and ZrO_2, highlighting that while silica negatively affects sodium corrosion resistance, Al_2O_3 enhances chemical stability in sodium and halide environments. Notably, alumina is the ceramic used in the ZEBRA battery (Na-$NiCl_2$) [33–35] due to its excellent corrosion resistance. BaO primarily modulates CTE and T_g, whereas ZrO_2 can influence the halide resistance of the sealing glass, by forming a zirconium hydroxide protective layer, which may function as a barrier to ionic diffusion and is believed to control the early stages of sealing glass degradation. Conversely, Suffner J. reported in his patent [36] that ZrO_2, while beneficial for chemical stability, can act as a nucleation site for crystalline phases, potentially leading to leakage in glass-ceramics. The patent suggested that fully vitreous sealants might be preferable for sodium-halide batteries and that incorporating inorganic fillers such as MgO, Al_2O_3, or stabilised ZrO_2 could optimise the sealant's thermal expansion, corrosion resistance, and flow properties.

To enhance bond strength between glasses and metals, the formation of an oxide layer on the metal through controlled pre-oxidation has been shown to significantly improve bonding compatibility with ceramic or glass substrates by enhancing interfacial wetting and chemical bonding [37,38]. In this context, Fe-Ni alloys also require careful pre-oxidation treatments to enable effective joining to ceramics or glass. A controlled heat treatment can help refine the oxide microstructure and improve oxide adhesion, thereby minimising crack formation within the oxide layer that could weaken the bond. In particular, for Fe-Ni metal alloys, Chern T.S. and Tsai H.L [39]. examined optimal pre-oxidation and sealing parameters for bonding Kovar to borosilicate glass. They found that pre-oxidation at 700 °C for 5-15 min produces a compact and dense iron oxide layer. Subsequently, the sealing process was carried out at 900 °C for 15 min. Similar findings were reported by Zanchetta A. et al. [40] and Kuo C. et al. [41], who successfully joined porcelain and silicate glasses to pre-oxidised Kovar. Conversely, research on the oxidation behaviour of Invar 36 and Invar 42 remains limited. The limited studies available in the temperature range 700 °C and 950 °C indicate that oxidation-induced mass gain becomes significant above 700 °C, resulting in the formation of Hematite (Fe_2O_3), Magnetite (Fe_3O_4), FeO, and $FeNi_3$, which are indicative of protective scale formation within this temperature range [42]. More recently, high-temperature oxidation studies by Zhang et al. [43] on Invar alloys revealed the formation of multi-layer oxide scales composed of Fe and Ni oxides, with the oxidation mechanism strongly dependent on temperature and microstructural features. It is worth noting that most experimental pre-oxidation studies focus on generic Fe/Ni alloys, and that the underlying mechanisms (scale nucleation, adhesion, formation of protective oxides), as well as the methodologies, are transferable to Invar42; however, understanding the native oxide stack is essential before designing a pre-oxidation to create a protective scale. Methods and temperatures reported in the literature therefore provide a starting point for Invar trials; nevertheless, only a few publications specifically address pre-oxidation treatments of Invar42.

As mentioned above, although silica-containing glasses are widely used as sealing materials, previous studies indicate that high SiO_2 contents may negatively affect chemical durability in sodium-rich environments [28,32]. For this reason, low-silica and silica-free compositions have been proposed as potential alternatives to improve corrosion resistance. However, their applicability to metal–ceramic joining systems, particularly for components in molten salt batteries, remains largely unexplored. In this context, the present work compares a commercial silica-based glass with a newly developed silica-free composition, aiming to assess the balance between chemical durability, thermo-mechanical compatibility, and structural stability during joining and ageing. Furthermore, the combined effects of controlled pre-oxidation of Invar alloys, silica-free glass formulations, and composite sealant strategies tailored for operation at 500–600 °C have not been systematically investigated.

The novelty of the present work lies in: (i) the application-oriented design of composite glass-based sealants for Invar42/Al_2O_3 joints operating under Na–Zn battery conditions; (ii) the direct comparison between a commercial silica-containing glass and a newly developed silica-free Y_2O_3–Al_2O_3–B_2O_3–BaO composition, both modified with alumina fillers; (iii) the use of in-situ high-temperature XRD to rationally select the pre-oxidation temperature for Invar42; and (iv) the correlation between oxide scale characteristics, interfacial microstructure, thermal stability, and shear strength performance. By integrating compositional design, interfacial engineering, and mechanical assessment under relevant thermal conditions, this study provides new insights into the reliability and limiting factors of Invar–ceramic joints for molten-salt battery systems.

2. Experimental

In this work two glass-based sealants were evaluated as possible candidates to join Invar42 metal alloy (Ni 41 wt% and Fe representing the balance, provided by VS & S s.r.l., Mesero, MI, Italy) and Al_2O_3 (99.8% ultra-high purity recrystallised Alumina provided by Nanovision S.r.l, Brugherio, MB, Italy) components of a Na-Zn liquid cell prototype, in the frame of the European SOLSTICE project (www.solstice-battery.eu): (i) the G018-402 commercial silica-based glass (referred to as SG) supplied by SCHOTT AG (Landshut, Germany), and (ii) a newly developed silica-free glass, containing Y_2O_3 as network modifier (referred to as YABB). The new Y_2O_3-Al_2O_3-B_2O_3-BaO glass system, was developed with the support of SciGlass Next (www.sciglass.uni-jena.de) database, driven by the following criteria: glass transition temperature (T_g) of the sealant that exceeds the operating temperatures of the cell (500 °C) and CTE closely matched with those of the substrates, α-Al_2O_3 ($\approx 7.6 \times 10^{-6}$ K^{-1} in the range RT-500 [44]) and Invar42 alloy ($\approx 6.7 - 7.4 \times 10^{-6}$ K^{-1} in the range of RT-450 °C). This glass was produced by conventional melting and casting techniques using high-purity grade raw materials: Y_2O_3 (Sigma Aldrich, 99.99% purity), Al_2O_3 (Alfa Aesar, 99.9% purity), B_2O_3 (precursor H_3BO_3, Sigma Aldrich, 99% purity), and BaO (precursor Ba_2CO_3, Thermoscientific, 99.8% purity). The raw material powders were mixed for 24 h and then melted in a Pt–Rh crucible using an electric furnace (LHT418PN2, Nabertherm GmbH, Lilienthal/Bremen, Germany) in air at 1350 °C for 1 h (with a lid covering the crucible) and then at 1400 °C for 30 min (without lid). Subsequently, the melt was cast onto a metal plate, ball-milled, and sieved to obtain a particle size $\leq$38 μm. The oxide compositions of the SG commercial glass [45] and the new YABB are reported in Table 1. To potentially enhance the Na corrosion resistance, alumina microfine powder (>99.5% purity, with a

Table 1
Chemical composition in wt% of the starting SG [45] and YABB glasses.

Raw materials	SG (wt%) [45]	YABB (wt%)
SiO_2	40-50	-
B_2O_3	>25-30	36
Al_2O3	17-25	27
Na_2O	5-15	-
MO (MgO + CaO + SrO + BaO)	<2	24 (BaO)
Others (ZnO + TiO_2+SnO_2)	0-5	-
Y_2O_3	-	13

grain size distribution of D50 = 3 μm) was added to both the glass systems, producing the SG-25A (referred to GA in a previous work by F. D'Isanto et al. [34]) and YABB-25A composite sealants (Table 2). In both systems, the powders were mixed with a laboratory roller mixer for 24h after the addition of Al_2O_3.

Both the parent SG and YABB, and the SG-25A and YABB-25A composite sealant systems obtained after the addition of alumina powder, underwent thermal characterisation using differential scanning calorimetry (DSC) and hot-stage microscopy (HSM) to establish optimal conditions for the joining process. DSC analyses (DSC 404 F1/F3 Pegasus instrument from Netzsch, Selb, Germany) were performed to examine the crystallisation behaviour from room temperature up to 1200 °C. HSM measurements (EM 301, Hesse Instrument, Harzgerode, Germany) were performed to assess the sintering behaviour of the glass systems. The HSM specimens were cylindrical pellets (3 mm in diameter and 3 mm in height) prepared by uniaxial pressing of glass powder with a few drops of ethanol. During testing, each pellet was placed on an alumina support and heated from room temperature up to the melting point identified by the instrument. Based on the observed shape and size changes during heating, the system automatically identified six key temperatures related to deformation and flow: (i) T_{fs}, the temperature at which the linear shrinkage of the glass begins; (ii) T_{ms}, the temperature at which this linear shrinkage reaches its maximum; (iii) DT, the temperature at which the initial signs of softening are observed; (iv) Sphere Temperature (ST), defined as the point at which the height of the sample equals the width of its base; (v) Half-Ball Temperature (HT), the temperature at which the sample height is reduced to half the width of the base; and (vi) Flow Temperature (FT), the temperature at which the sample height falls below one-third of the base width. All measurements were performed at a heating rate of 5 °C/min in a flowing air atmosphere.

Sandwich-like structure samples were prepared using the investigated glass-based sealants, following the scheme shown in Fig. 1a and b. A slurry paste composed of water (approximately 30 wt%) and powders (approximately 70 wt%) was manually deposited with a spatula between α-Al_2O_3 and Invar42 to be joined. Before the deposition, a pre-oxidation thermal treatment was performed on the Invar42 metal parts. To study the influence of different temperatures on the oxide scale, three Invar42 specimens were heated by X-ray diffraction (H-XRD) in a hot chamber to 650, 700, and 750 °C, respectively, with an isotherm of 10 min, followed by cooling to ambient temperature. H-XRD was performed using an Empyrean, III serie, Malvern Panalytical diffractometer (Philips, Almelo, The Netherlands), with Cu Kα radiation and the HTK1200N, Anton Paar hot chamber. Phase identification was performed using X-Pert HighScore software and the JCPDS database from ICDD (International Centre for Diffraction Data, Newton Square, Pennsylvania, USA).

Based on the results from the DSC and HSM analyses, the sandwich-like samples were subjected to the joining thermal treatment at 900 °C for 40 min (SG-25A system) and 900 °C for 1h (YABB-25A system). Both these treatments were carried out at a heating/cooling rate of 5 °C/min in air.

A field-emission scanning electron microscope (FE-SEM, MIRA3 XMH, TESCAN, Czech Republic) equipped with an energy-dispersive spectrometer (EDS, Ultim Max 40, Oxford Instruments, UK) was used for the morphological and chemical characterisation of the joined samples. Before the SEM investigation, the cross-sectioned samples were polished using SiC papers from grit size 120 to 4000. Finally, the non-conductive samples were sputtered with Pt to make the surface electronically conductive.

Table 2
Glass and composite sealant systems.

Glass	Glass (wt%)	Al_2O_3 (wt%)
SG	100	-
SG-25A	75	25
YABB	100	-
YABB-25A	75	25

The thermal expansion coefficient (CTE), glass transition temperature (T_g) and dilatometric softening temperature (T_d) of the YABB-25A sealant after the joining thermal treatment were determined by dilatometry (Netzsch DIL 402 PC) at a heating rate of 5 °C/min. XRD analysis was carried out on the glass-based sealant obtained after the joining thermal treatment, and the measurement were conducted between 10° and 70° using the previously mentioned diffractometer.

The apparent shear strength of Invar42/Al_2O_3 and Al_2O_3/Al_2O_3 joined samples was determined through single lap offset (SLO) tests conducted under compression, following a methodology adapted from ASTM D905-08 [46]. The specimens for mechanical evaluation were produced according to the configurations illustrated in Fig. 2a and b. The testing fixtures were arranged to minimise substrate bending and rotation, as described in Ref. [47] (see Fig. 2c). Mechanical testing was performed using a universal testing machine (Syntec D/10, MTS Corp.) equipped with a 50 kN load cell, applying a crosshead displacement rate of 0.5 mm/min. The peak force during testing was recorded, and the apparent shear strength was calculated by dividing this maximum force by the area of the joint. The dimensions of the single lap offset specimens were 15 mm × 10 mm × 3 mm. Fracture surfaces of selected samples were examined and characterised macroscopically.

3. Results and discussion

3.1. Pre-oxidation of Invar42 metal substrates

The development of an oxide layer on the metal surface, induced by heat treatment, has been shown in the literature to markedly enhance wetting behaviour and thereby strengthen the adhesion between glass and metal [37,38]. For this purpose, three Invar42 samples were subjected to an H-XRD analysis at 650, 700 and 750 °C, respectively. The diffraction patterns are shown in Fig. 3. For reference, the diffractogram of the Al_2O_3 sample carrier (identified by the PDF card n. 01-081-2266) is also reported to facilitate the identification of the carrier-related peaks, which are visible in nearly all specimens. The Invar42 diffraction pattern before the oxidation heat treatment is also reported (labelled RT in Fig. 3a), showing the presence of the iron nickel phase ($Fe_{0.64}Ni_{0.36}$, PDF card n. 00-047-1405). In line with what was observed in previous studies on Fe-Ni alloys [39,40], two crystalline phases referred to rhombohedral Fe_2O_3 (Hematite, PDF card n. 01-088-2359) and cubic Fe_3O_4 (Magnetite, PDF card n. 03-065-3107) were identified on the samples after heating at 650, 700 and 750 °C. These phases are typical of the first stage of oxidation of iron-nickel alloys [42] and it can be pointed out that the intensity of the Fe_2O_3 peaks increases as the temperature increases. The slight shift toward lower 2θ values observed in the high-temperature diffraction patterns (as shown in the magnified view in Fig. 3b) can be ascribed to the thermal expansion of the crystal lattice at elevated temperature, followed by its contraction upon cooling back to room temperature.

On the basis of these results, a pre-oxidation temperature of 700 °C was selected for subsequent experiments. At this temperature, the formation of a continuous oxide layer is clearly evidenced by the presence of both hematite and magnetite phases, while avoiding excessive oxide growth and spallation observed at higher temperatures [42]. High-temperature oxidation studies on Fe–Ni based alloys indicate that the oxidation rate and oxide scale thickness increase significantly with temperature. For example, oxidation of Fe–Ni–Cr alloys at 800 °C and 900 °C yields much higher parabolic rate constants and more rapid scale growth than at 700 °C, suggesting that temperatures above ~700 °C can lead to uncontrolled oxide growth, increased porosity, and greater risk of scale spallation upon cooling [48]. Moreover, 700 °C is a temperature sufficiently low to preserve the bulk microstructure and the characteristic low thermal expansion of the Invar alloy, in agreement with

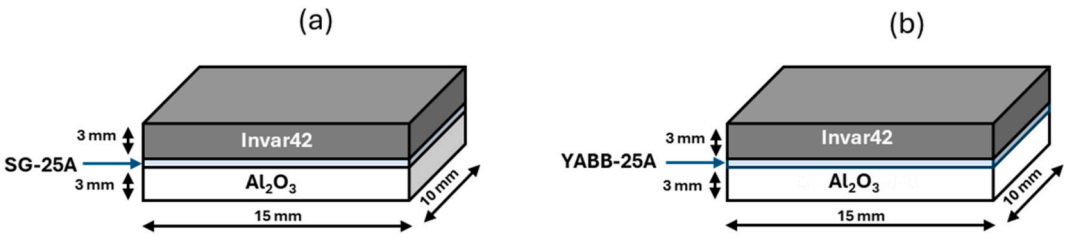


Fig. 1. Schematic representation of sandwich-like samples with (a) SG-25A and (b) YABB-25A composite sealants as joining material.

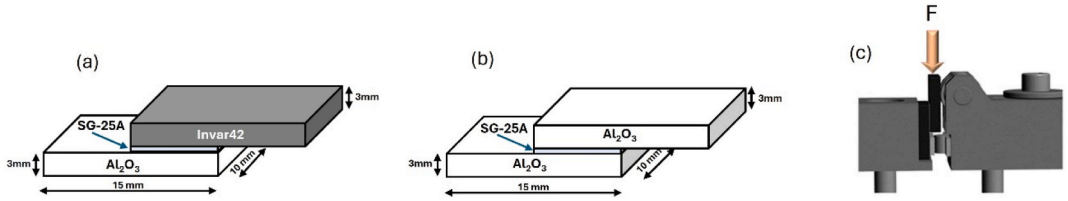


Fig. 2. (a) Schematic representation of (a) dissimilar and (b) similar as-joined samples for single lap offset (SLO) mechanical test. (b) Configuration of the fixtures to avoid bending and rotation of the substrates during the test.

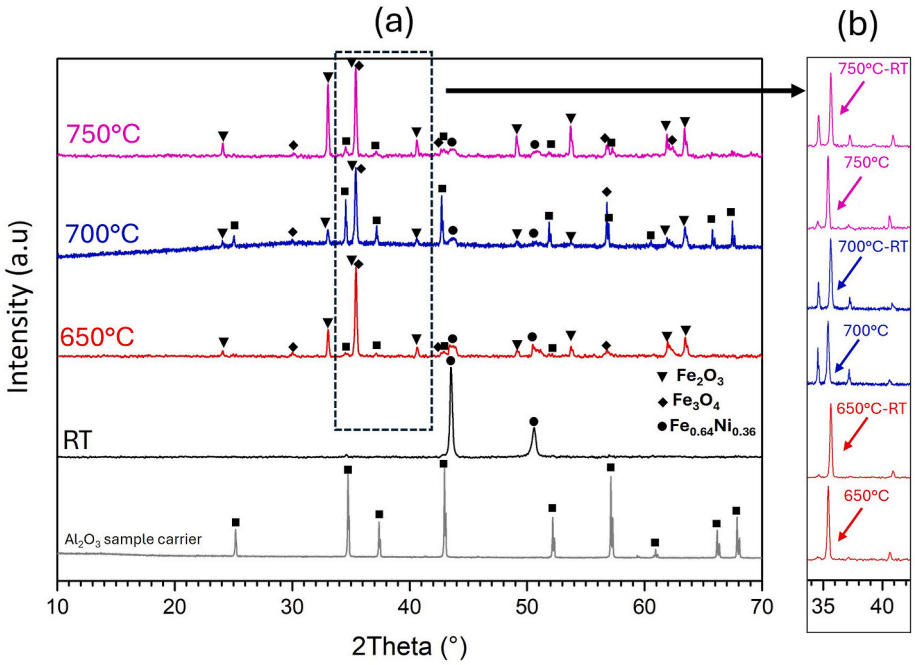


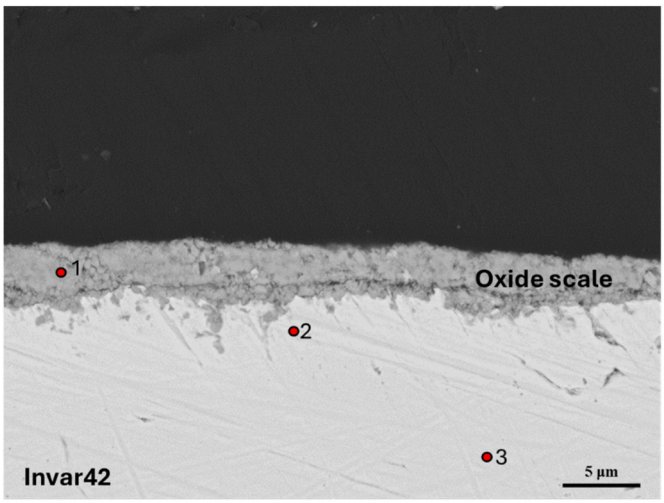
Fig. 3. (a) X-ray diffraction patterns of the Al_2O_3 sample carrier, Invar42 prior to oxidation heat treatment (RT) and Invar42 oxidised at 650, 700 and 750 °C for 10 min (patterns stacked from bottom to top); The dashed box highlights the 2θ region selected for detailed analysis. (b) Magnified view of the boxed area in (a) comparing the XRD patterns collected at the end of the heat treatment and after cooling back to room temperature (RT).

previous studies on Fe–Ni systems [49].

From a morphological point of view, the oxide scale formed after the pre-oxidation treatment at 700 °C for 10 min was characterised using FE-SEM coupled with EDS analysis. The results are reported in Fig. 4. The oxidised sample exhibited a homogeneous iron oxide layer with an average thickness of approximately 5 μm. Moreover, the EDS analysis revealed the presence of an Fe-depleted region in the metal adjacent to the oxide scale, in good agreement with previous observations reported by Zanchetta et al. for a FeNiCo alloy [40].

3.2. Characterisation of glass-based sealants

Fig. 5 shows the experimental data obtained from DSC and HSM analyses on the SG/SG-25A and YABB/YABB-25A glass-based systems, respectively. The characteristic temperatures (T_g, T_x, T_p) for all systems under study were extrapolated from the DSC curves in Fig. 5a and b and reported in Table 3. One can observe that, for SG and SG-25A, no transformation was detected other than the glass transition in both glasses. The onset T_g was measured equal to 478 °C for SG and 482 °C for SG-25A, respectively. The absence of devitrification phenomena suggested that both formulations are expected to show excellent thermal stability, with no modification in the materials' structure over the temperature range of operation and sealing. On the other hand, Fig. 5b revealed a T_g of 609 °C for YABB glass and 625 °C for YABB-25A. YABB glass-based systems showed two exothermic peaks related to crystallisation, corresponding to 880 °C and 1057 °C in YABB glass and 887 °C



at%	O	Fe	Ni
1	61.4	38.0	0.6
2	-	33.9	66.1
3	-	58.7	41.3

Fig. 4. FE-SEM cross-sectional micrograph of Invar42 oxidised in a chamber furnace at 700 °C for 10 min. The EDS analyses corresponding to the points indicated in the figure are reported in the table below.

and 1060 °C in YABB-25A. These comparable peak temperatures indicate that the 25 wt% Al_2O_3 addition does not significantly affect the crystallisation behaviour of the base glass. The sintering behaviour of the SG and SG-25A [34] and YABB and YABB-25A systems was analysed with hot stage microscopy, with a comparison of the pure glass versus the glass with the addition of alumina powder in Fig. 5c and d, respectively. The graphs show the linear shrinkage as a function of temperature, from room temperature to the flow point identified by the instrument. Furthermore, Fig. 6 presents the key characteristic temperatures identified during the HSM analyses [50]. The most evident aspect of the graphs in Fig. 5c and d is that the behaviour of the glass matrix mainly governs it, while the onset of sintering (T_{fs}) is only marginally affected by the presence of alumina powder and is mainly governed by the behaviour of the glass matrix, a different trend emerges as sintering progresses. In particular, the maximum shrinkage temperature (T_{ms}) increases from 720 °C in SG to 790 °C in SG-25A [34], and from 734 °C in YABB to 797 °C in YABB-25A. Indeed, as densification advances, the related phenomena are strongly affected by the matter's viscous flow, which is, however, reduced by the friction between the glass mass and the alumina powders. Overall, both composite systems exhibited a systematic shift of the characteristic temperatures (T_{ms}, DT, ST, HT, and FT) toward higher values, indicating a reduced ability to undergo shrinkage by viscous flow. Neither the silica-based nor the silica-free composite compositions reached the flow temperature within the investigated range, up to 1400 °C. This behaviour is attributable to the higher effective viscosity introduced by the Al_2O_3 particles, which restricts further densification and results in a relative shrinkage slightly above 30% for both sealants.

Furthermore, a plateau in the YABB/YABB-25A system at 800 °C may be explained by an increase in viscosity due to devitrification, which began after 831 °C, as noted in the DSC-identified characteristic temperatures (T_x in Table 3).

Based on thermal analyses, SG-25A and YABB-25A glasses were selected as sealing candidates for joining Invar42 to Al_2O_3 in all-liquid Na–Zn battery prototypes. This choice was motivated by the

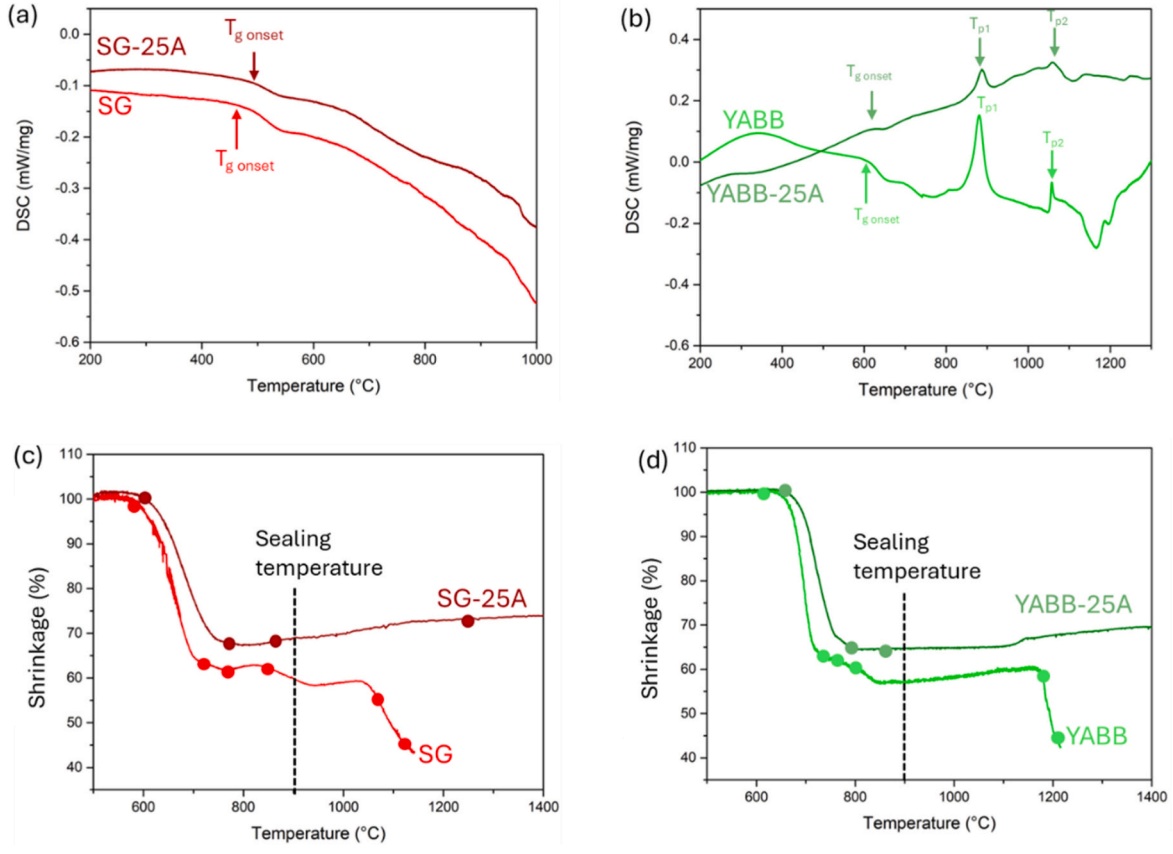


Fig. 5. DSC and HSM of (a,c) SG and SG-25A and (b,d) YABB and YABB-25A glass-based compositions.

Table 3
Characteristic temperatures of SG, SG-25A, YABB, YABB-25A systems; all data were obtained by DSC and dilatometric analyses.

Characteristic temperatures	SG	SG-25A	SG-25A Sealant (900 °C 1h)	YABB	YABB-25A	YABB-25A Sealant (900 °C 1h)
$T_{g\ onset}$ (°C) (DSC)	478	482	-	609	625	-
T_{x1} (°C) - T_{x2}(°C)	-	-	-	831-1049	860-1050	-
T_{p1}(°C) - T_{p2}(°C)	-	-	-	880-1057	887-1060	-
T_g (DIL)	-	-	511[34]	-	-	541
T_d (DIL)	-	-	603 [34]	-	-	588

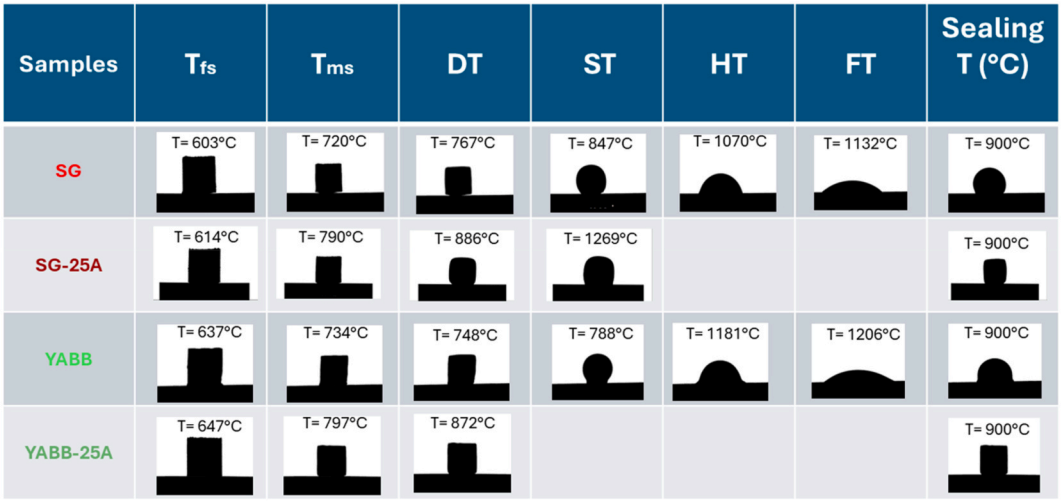


Fig. 6. Images of characteristic temperatures at fixed viscosity values detected by the hot stage microscope during heating from room temperature to the flow temperature(T_{fs}, T_{ms}, DT, ST, HT, FT) for the glass-based compositions under study (SG-25A data were adapted by Ref. [34]). The images of the sample at the selected sealing temperature for all the glass-systems (900 °C) are also shown.

composite approach, which allows for higher characteristic temperatures and provides improved resistance to corrosive environments. The thermal treatment used to consolidate the joining materials was performed at 900 °C for 40 min for SG-25A [34] and at 900 °C for 1 h for YABB-25A. The silica-containing glass, as previously demonstrated for the same composition (denoted GA) [34], after the joining thermal treatment at 900 °C for 40 min remains amorphous, with XRD patterns showing the absence of any crystalline phases except the alumina added in the form of powder. On the other hand, in the XRD analysis carried out in this study on the silica-free glass system after the joining thermal treatment (Fig. 7), the formation of three distinct crystalline phases emerged. Specifically, yttrium borate (YBO_3), assigned based on the 01-089-3501 PDF card, and aluminium borate (Al_5BO_9), attributed using the 01-072-1931 PDF card, were detected as the main phases. Both phases have been previously reported by Deters H. and Eckert H [51]. in similar glass systems. In addition, barium yttrium oxide ($Ba_4Y_2O_7$) identified by the 00-037-0992 PDF card, was observed as a minor phase. The presence of the peaks referred to alumina is clearly detectable in the glass-based sealant by the 00-010-0173 PDF card corresponding to the rhombohedral Corundum aluminium oxide.

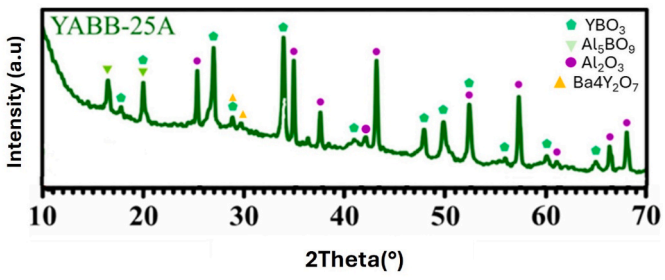


Fig. 7. XRD diffractogram of the YABB-25A after the joining thermal treatment at 900 °C for 1h.

To thermomechanically characterise the glass-based sealants under study, dilatometric measurements were performed on glass pellets after the joining thermal treatment and the results are shown in Table 3). Dilatometry of SG-25A in Fig. 8, adapted from Ref. [34], showing an experimentally measured CTE of ~7.3•10^{-6} K^{-1} (100-300 °C), while the YABB-25A dilatometric curve (Fig. 8) resulted in a CTE value of 7.2•10^{-6} K^{-1} (40-450 °C). These values are very close to those of Invar42 (6.7- 7.4•10^{-6} K^{-1}) in the same range of temperature [52], as well as those of the alumina (7.6•10^{-6} K^{-1} in the range 40-500 °C) [44].

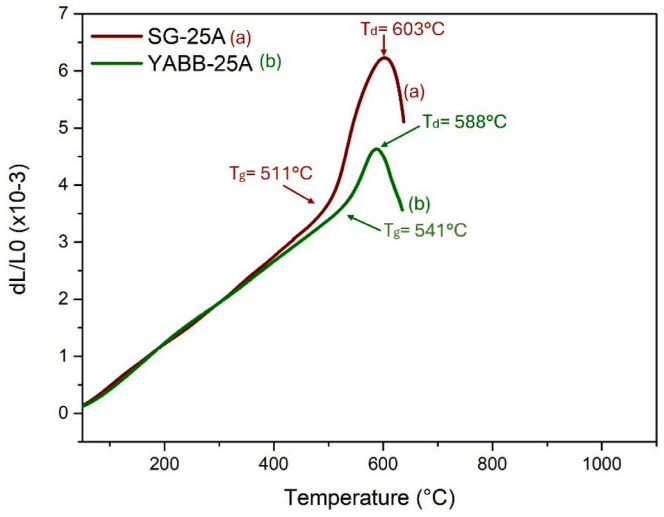


Fig. 8. Dilatometric curves of (a) the SG-25A (adapted from Ref. [34]) and (b) YABB-25A sealants after the joining thermal treatments at 900 °C for 40 min and 900 °C for 1 h, respectively. The characteristic temperatures T_g and T_d identified from the curves are also indicated in the figure.

Furthermore, from the dilatometric curves it was reported, a T_g and T_d equal to 511 °C and 603 °C, respectively, for the SG-25A after thermal treatment at 900 °C for 40 min [34], and a T_g and T_d of 541 °C and 588 °C, respectively, for YABB-25A, after thermal treatment at 900 °C for 1h. The reduction in T_g of YABB-25A, from 625 °C before the joining thermal treatment to 511 °C after the sinter-crystallisation joining process, can be attributed to the preferential retention of Ba in the amorphous phase, while alumina and yttria are mainly incorporated into the two principal crystalline phases. The enrichment of Ba in the glassy phase acts as a network modifier, thereby lowering the T_g [53,54]. In any case, both the sealants proposed resulted in a softening temperature higher than the operating temperature (500 °C).

3.3. Characterisation of Invar42/Al_2O_3 joined samples

A pre-oxidation treatment on Invar42 metal substrates, consisting of heating up to 700 °C, followed by an isothermal treatment for 10 min, was performed prior to the joining process. After that, the following sandwich-like specimens were produced with the scheme of Fig. 1a and b, using the joining procedure described in the experimental section: Invar42/SG-25A/Al_2O_3 and Invar42/YABB-25A/Al_2O_3. The thermal treatment to consolidate the joining material was chosen to ensure a viscosity suitable for effective glass flow and adequate sinter-ability on the Invar42 and Al_2O_3 substrates. Figs. 9a and 10a show the results of the FE-SEM characterisation of the cross-section of the Invar42/SG-25A/Al_2O_3 and Invar42/YABB-25A/Al_2O_3 joined samples. From a morphological point of view, the cross-sections of both samples revealed the effectiveness of the sealing material in forming well-adhered, crack-free joints with the selected substrates. Although no cracks were detected in the composite sealant, demonstrating good thermo-mechanical matching between the sealant and the substrates, the microstructure revealed the presence of closed porosities within the glass sealant (Fig. 9a). These pores could be attributed to the manual deposition of the slurry and to the relatively high viscosity of the composite at the sealing temperature, which may partially hinder gas escape before complete densification. The observed porosities are isolated and not interconnected; therefore, they do not compromise the macroscopic integrity or continuity of the joint. Their presence is therefore associated with processing-related factors rather than with interfacial debonding.

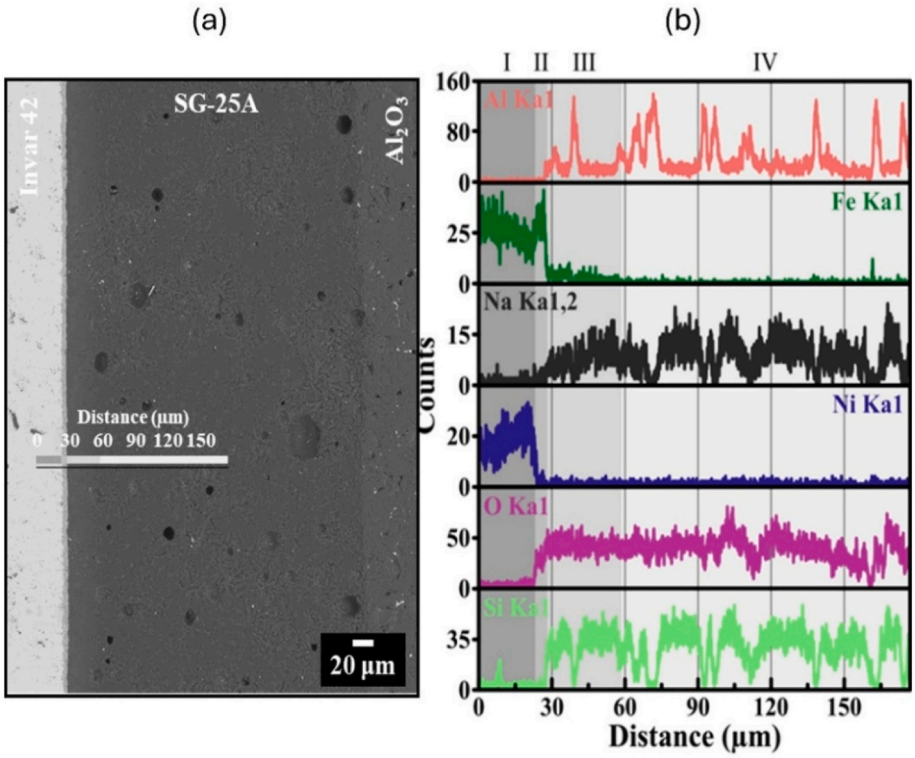
To specifically evaluate the chemical composition of the joined area, FE-SEM analysis coupled with linear EDS analysis (Figs. 9b and 10b) revealed four distinct compositional zones in both the Invar42/SG-25A/Al_2O_3 and Invar42/YABB-25A/Al_2O_3 joined samples: i) the Invar42 substrate; ii) the iron oxide scale; iii) the Fe diffusion region from the metal into the glass matrix of the composite sealant; iv) the composite sealant.

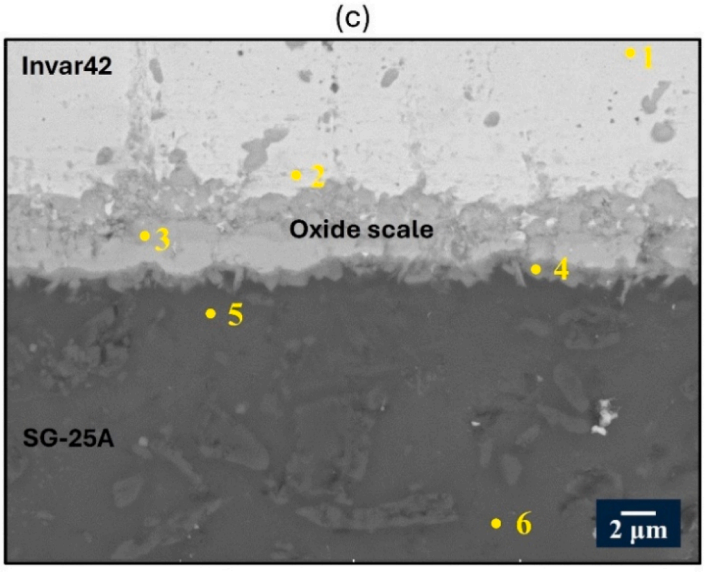
EDS analysis reported in Fig. 9b confirms the presence of a thin iron oxide scale on the surface of the metallic substrate, with a thickness of approximately 5.5-6.0 μm. Moreover, the area of diffusion of iron oxide into the glass was detected about 30 μm. A higher magnification FE-SEM analysis at the Invar42/oxide scale and oxide scale/glass sealant interfaces of the Invar42/SG-25A/Al_2O_3 is shown in Fig. 9c. At the same time, the chemical composition detected by the EDS was reported in the corresponding table. The characterisation shows the presence of a double layer of oxides, one inner (point 3) predominantly composed of Fe and O, and one in contact with the glass (point 4) which contains detectable amounts Al, which can be attributed to diffusion from the glass sealant during the joining process. Furthermore, Fe depletion in the metallic substrate adjacent to the oxide scale is evident at point 2 when compared with point 1, reflecting outward diffusion of Fe during oxidation and subsequent scale growth.

As it can be observed in Fig. 10a, during the joining process, the YABB-25A glass developed crystalline phases, identified by the XRD analysis in Fig. 7. Also in this case, the linear EDS analysis (Fig. 10b) revealed the presence of an area close to the oxide scale, where some Fe was detected. In this case, the Fe diffusion region was more pronounced within approximately 30 μm inside the glass, and gradually decreased up to about 60 μm. The EDS analysis of the interface between Invar42 and the YABB-25A sealant (Fig. 10c) indicates that with this silica-free glass, the oxide scale evolved differently. The two oxide phases, one predominantly composed of Fe and O (point 3) and the other containing Al along with some Ni (point 2), do not appear as distinct, successive layers. Instead, the Fe-O-rich phase is embedded into the Al- and Ni-containing oxide phase. In addition, the oxide scale is significantly thinner than in the SG-25A system, with an estimated thickness of approximately 2.5 μm. Furthermore, the EDS analysis performed on the sealant revealed the presence of at least 3 different phases, which the authors attempted to correlate with those identified by X-ray diffraction in Fig. 7: the yttrium borate, probably corresponding to the light spikes of point 6, and the aluminium oxide borate, corresponding to the darker areas of point 5, which were surrounded by the glass matrix (point 4) enriched by Fe, as previously observed. However, a clear one-to-one correlation could not be achieved, consequently, further detailed investigations (e.g. EDS analyses at higher magnifications) will be required to better understand the nature, distribution, and origin of these phases.

Both the Invar42/SG-25A/Al_2O_3 and Invar42/YABB-25A/Al_2O_3 joined samples were subjected to an aging test consisting of heating at 600 °C for 150h to test the reliability of the joining at temperature higher than the operating one (500 °C). The samples joined with the YABB-25A failed during the test, and this can be interpreted in terms of residual thermoelastic stresses generated by the sinter-crystallisation process. XRD analysis revealed the formation of crystalline phases, including Al_5BO_9, which exhibits intrinsically anisotropic thermal expansion [55]. Although randomly oriented crystallites may yield an apparently isotropic macroscopic CTE, anisotropic lattice expansion at the grain scale still produces local strain mismatch between crystalline phases and the residual glassy matrix. In glass-ceramic systems, crystallisation introduces heterogeneity in elastic modulus and thermal expansion, leading to residual internal stresses during cooling and subsequent thermal exposure [53]. In a mechanically constrained sealing layer configuration joined to dissimilar substrates, such stresses cannot be fully relaxed and may promote microcrack nucleation at crystal/glass and crystal/crystal interfaces. Progressive coalescence of these microcracks can ultimately result in macroscopic cracking of the joint. Therefore, the reduced reliability of the YABB-25A system may be attributed to crystallisation-induced microstress within a mechanically constrained glass-ceramic interlayer rather than to a purely macroscopic anisotropic CTE effect.

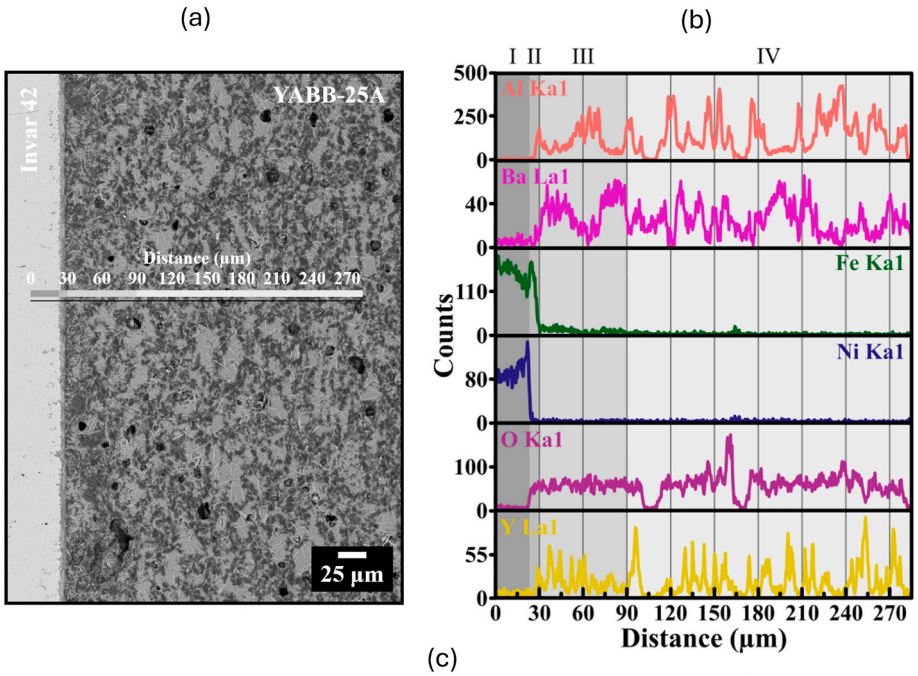
On the other hand, the sample joined with the SG-25A glass demonstrated satisfactory stability during thermal aging for 150h at 600 °C. As shown in Fig. 11, which presents the FE-SEM cross-section (Fig. 11a) and the corresponding linear EDS profile (Fig. 11b) of the Invar42/SG-25A/Al_2O_3 after ageing, the morphology and oxidation scale thicknesses remain essentially unvaried compared to the one observed for as-joined sample. This confirms that the SG-25A composite sealant was effective in forming continuous, well-bonded, and defect-free interfaces with the selected substrates. A higher-magnification FE-SEM image of the Invar42/SG-25A interface is added in the inset of Fig. 11a, with the corresponding EDS elemental analysis in Fig. 11c. The results confirm that a bilayer oxide structure persists even after thermal ageing. Since the promising results obtained with the ageing test, an Invar42/SG-25A/Al2O3 specimen was also cycled two times, reaching the temperature of 600 °C, which was maintained stable for 2h before cooling at 5 °C/min down at room temperature. The cross-section of the sample is shown in Fig. 11d, and its chemical composition was analysed by linear EDS (Fig. 11e), both showing no detectable variations compared with the thermal aged specimen. The oxide scales formed after the thermal treatment were demonstrated to maintain substantially the same morphology and thickness. The last traces of Fe were detected at about 25 μm from the oxide scale after ageing (Fig. 11c, points 1 and 4) and after cycling (Fig. 11f, points 10 and 11), which is similar to the

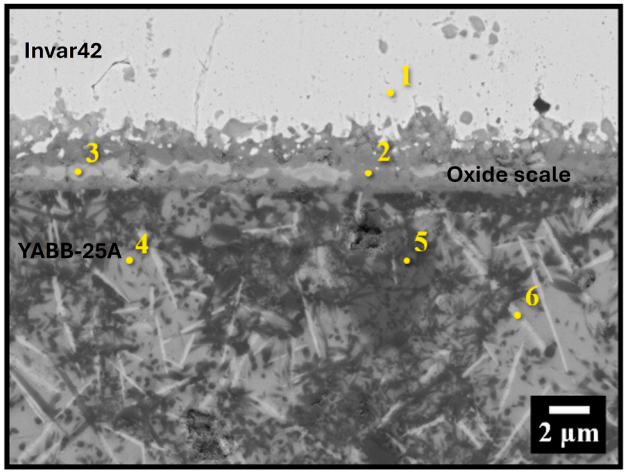




at%	1	2	3	4	5	6
O	-	-	56.7	59.9	68.3	70.7
Na	-	-	0.5	0.7	4.1	5.5
Al	-	-	0.6	16.7	11.6	7.7
Si	-	-	0.2	1.0	12.4	14.9
Fe	57.9	41.9	41.6	21.6	3.6	1.3
Ni	42.1	58.1	0.4	-	--	-

Fig. 9. (a) BSE cross-sectional micrograph of the Invar42/SG-25A/Al_2O_3 joined sample and (b) line-scan EDS analysis acquired along the line indicated in (a). (c) Higher magnification of FE-SEM image of the Invar42/oxide scale and oxide scale/SG-25A sealant interfaces, together with the corresponding point EDS compositional analyses.





at%	1	2	3	4	5	6
O	-	15.8	11.7	22.9	30.7	25.8
Y	0.2	0.3	0.1	6.1	14.4	37.9
Al	0.3	6.2	0.6	13.4	37.1	9.0
Ba	0.1	1.5	0.6	46.5	7.8	21.3
Fe	35.4	71.3	86.1	11.2	9.7	5.7
Ni	64.0	5.0	0.9	-	0.4	0.3

Fig. 10. (a) BSE cross-sectional micrograph of the Invar42/YABB-25A/Al_2O_3 joined sample and (b) line-scan EDS analysis acquired along the line indicated in (a). (c) Higher magnification of FE-SEM image of the Invar42/oxide scale and oxide scale/YABB-25A sealant interfaces, together with the corresponding point EDS compositional analyses.

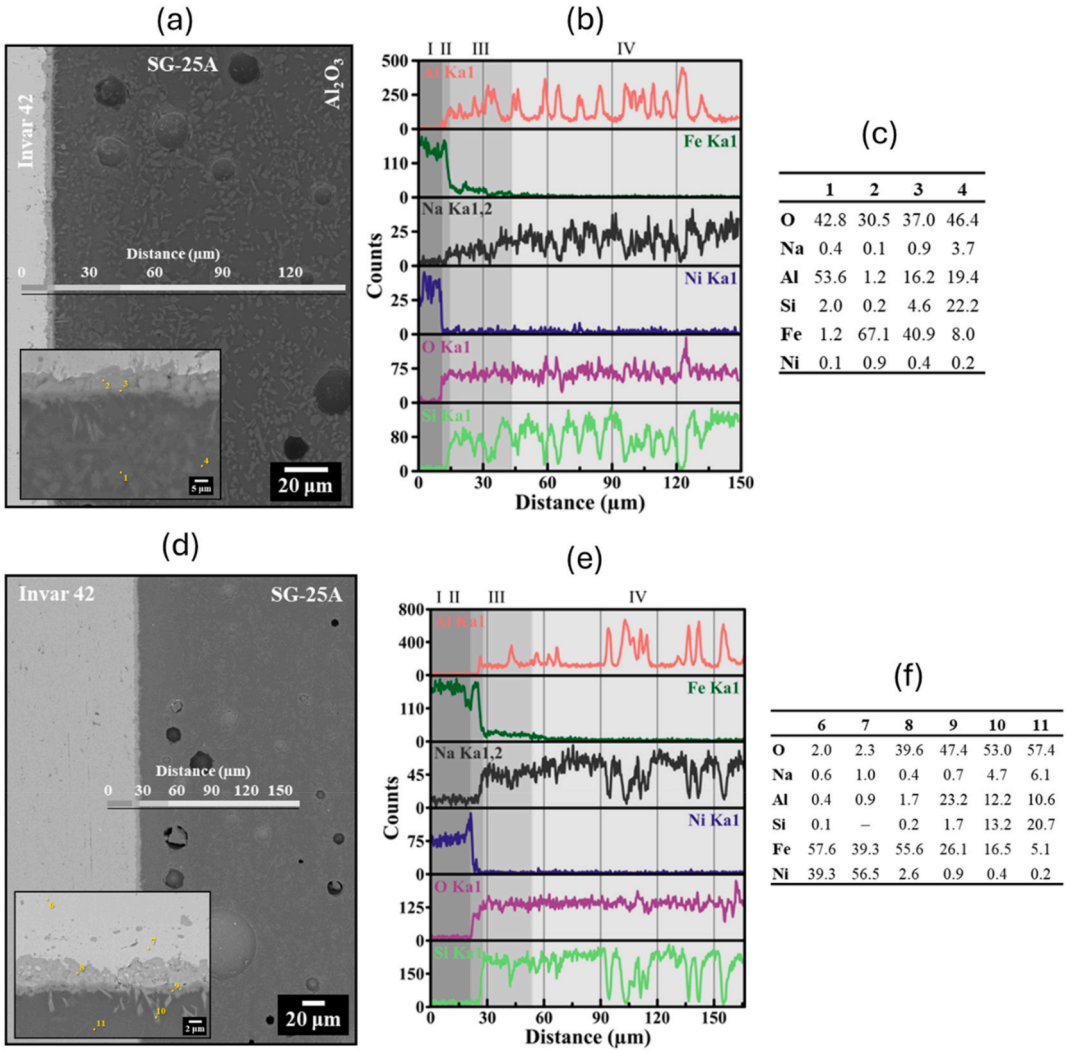
30 μm measured in as-joined samples (Fig. 9).

3.4. Single lap offset mechanical tests

Given the presence of cracks in the YABB-25A glass-based sealant after thermal ageing at 600 °C for 150 h, it was discarded as a joining material for the final application, while SG-25A was further characterised by mechanical testing as a potential candidate for application in the liquid metal battery prototype.

Due to the geometry of the final configuration of the cell, the joining area would be stressed by shear forces. For this reason, the mechanical shear test was performed on 3 specimens processed by joining pre-oxidised Invar42 to alumina using SG-25A slurry, following the configuration represented in Fig. 2a. As for the other samples, the joining thermal treatment was carried out at 900 °C for 40 min. The mechanical behaviour of these joints was evaluated, yielding an average apparent shear strength of 23 ± 7 MPa. The relatively large standard deviation indicates a non-negligible variability in joint performance, which can be attributed to two main concurrent microstructural factors.

First, fracture surface analyses revealed that failure predominantly



(c)

	1	2	3	4
O	42.8	30.5	37.0	46.4
Na	0.4	0.1	0.9	3.7
Al	53.6	1.2	16.2	19.4
Si	2.0	0.2	4.6	22.2
Fe	1.2	67.1	40.9	8.0
Ni	0.1	0.9	0.4	0.2

(f)

	6	7	8	9	10	11
O	2.0	2.3	39.6	47.4	53.0	57.4
Na	0.6	1.0	0.4	0.7	4.7	6.1
Al	0.4	0.9	1.7	23.2	12.2	10.6
Si	0.1	–	0.2	1.7	13.2	20.7
Fe	57.6	39.3	55.6	26.1	16.5	5.1
Ni	39.3	56.5	2.6	0.9	0.4	0.2

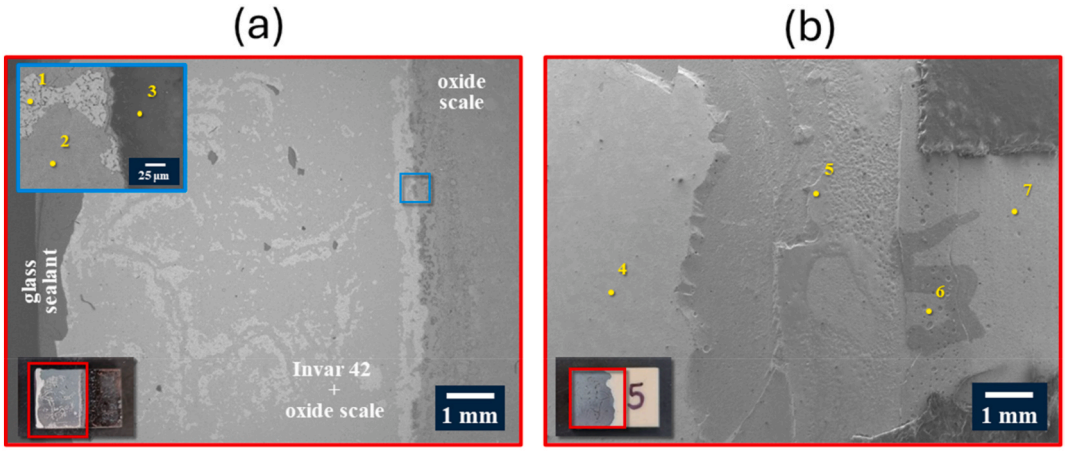
Fig. 11. (a, d) BSE cross-section micrographs of the Invar42/SG-25A/Al_2O_3 after ageing and after two thermal cycles at operating temperature, respectively; (b, e) line-scan EDS analyses acquired along the lines indicated in (a) and (d), respectively. Higher magnification views of the Invar42/oxide scale and oxide scale/SG-25A interfaces highlighted in the insets of (a) and (d) together with the corresponding point EDS compositional analyses in (c) and (f).

occurred within the iron oxide scale rather than through the bulk of the composite sealant. The oxide layer formed after pre-oxidation at 700 °C is approximately 5 μm thick and consists mainly of Fe_2O_3 and Fe_3O_4 phases. Due to its intrinsically brittle nature, this interfacial layer represents the mechanically weakest region of the joint. Local variations in oxide thickness, microstructural heterogeneities, and possible microcracks generated during cooling may strongly influence crack initiation. In such systems, where failure is controlled by a thin brittle interlayer, the measured strength is statistically governed by the most critical local defect, leading to an intrinsic scatter typical of brittle fracture processes.

Second, the presence of closed porosities within the composite sealant may contribute to strength dispersion. Although no macroscopic cracks were observed in the as-joined condition, isolated pores were detected within the glass matrix, which could be associated with manual slurry deposition and the relatively high viscosity of the composite during viscous flow at the sealing temperature. These pores can act as local stress concentrators under shear loading, promoting premature crack initiation in some specimens and thus increasing specimen-to-specimen variability.

To further elucidate this behaviour, the fracture surfaces were examined by FE-SEM (Fig. 12a and b) and EDS (Fig. 12c). The Invar42 side (Fig. 12a) displayed distinct regions identified by BSE contrast: two lighter zones are visible on the portion of the substrate that was joined to the alumina (points 1 and 2), corresponding to Fe-depleted Invar42, while darker areas correspond to the oxide scale. In particular, the darkest regions (point 3) containing Si, Al and Na appearing as isolated spots elsewhere, were attributed to the sealant. The broad dark-grey region near the joint interface, mainly composed of Fe and O, corresponds to remnants of the oxide scale. On the alumina counterpart (Fig. 12b), the joint area is largely covered by a glassy layer containing iron oxide particles on its surface (point 4). Additional regions (points 5 and 6) were identified as sealant residues, similarly to those detected on the Invar42 side. It can be assumed that adhesive failure occurs on the Invar42 side, with the fracture primarily propagating through the oxide scale and along the oxide/sealant interface.

A comparison with three alumina-to-alumina joints produced with SG-25A sealant provides additional insight. These joints exhibited a significantly higher average apparent shear strength of 52 ± 14 MPa, reflecting the better adhesion of the alumina–glass interfaces, since the fracture occurred jumping from one interface to another (adhesive/cohesive failure). The persistence of strength variability even in this configuration suggests that part of the scatter is process-related, likely associated with slurry deposition and residual porosity in the sealant. However, the substantially lower average strength of the Invar42-containing joints clearly identifies the pre-formed iron oxide scale as the limiting mechanical element governing failure. This emphasises the



(c)

at%	1	2	3	4	5	6	7
O	6.7	48.3	65.2	42.6	57.1	57.6	56.7
Na	–	–	4.4	–	3.7	3.2	–
Al	–	–	11.7	–	30.1	30.6	43.3
Si	–	–	13.7	–	9.1	8.6	–
Fe	40.5	46.5	5.0	57.4	–	–	–
Ni	52.8	5.2	–	–	–	–	–

Fig. 12. Fracture surface BSE micrographs of (a) the Invar42 and (b) alumina substrates of a Invar42/SG-25A/Al_2O_3 joined sample tested through SLO in compression with (c) chemical composition detected by EDS analysis.

need for improved control of the oxide scale formation and dissolution processes to enhance the mechanical performance and reliability of Invar–ceramic joints.

Overall, the results indicate that while the SG-25A composite sealant ensures good thermo-mechanical compatibility and interfacial bonding in the alumina-to-alumina system where it can sustain higher mechanical loads due to the absence of a weak interfacial iron oxide scale, the mechanical performance of Invar42/Al_2O_3 joints is primarily controlled by the fracture resistance and uniformity of the oxide scale formed during pre-oxidation. Although the YABB-25A system ultimately developed cracks after thermal ageing due to crystallisation-induced anisotropy, this outcome provides valuable insight. It highlights the trade-off between chemical durability and structural stability, suggesting that full silica-free systems may not provide sufficient resistance to crystallisation-induced stresses under the investigated conditions. These findings indicate that future optimisation may focus on low-silica (rather than silica-free) compositions, aiming to maintain high sodium corrosion resistance while improving structural and thermo-mechanical stability.

4. Conclusions

This work investigated the joining of Invar42 to alumina for high-temperature Na–Zn molten-salt battery applications using glass-based composite sealants. Controlled pre-oxidation of Invar42 at 700 °C produced a continuous iron oxide scale, enabling effective wetting and interfacial bonding with the glass sealants. Among the investigated systems, the silica-containing SG-25A composite demonstrated superior thermo-mechanical stability compared with the silica-free YABB-25A, which developed cracks after thermal ageing due to crystallisation-induced anisotropy.

Mechanical testing confirmed that SG-25A provides reliable bonding under shear loading, resulting in an average apparent shear strength of 23 ± 7 MPa. Nevertheless, the fracture resistance of the joint is primarily governed by the intrinsic brittle behaviour of the oxide scale at the metal–glass interface.

Overall, the results demonstrate that silica-containing glass-based composite sealants combined with controlled pre-oxidation represent a viable strategy for durable Invar–alumina joining in molten-salt battery environments. Further optimisation of oxide scale formation and deposition method may enhance mechanical reproducibility and long-term reliability. Future work will explore low-silica glass compositions to balance sodium corrosion resistance with improved structural and thermo-mechanical stability.

CRediT authorship contribution statement

F. D'Isanto: Writing – review & editing, Writing – original draft, Visualization, Investigation, Formal analysis, Conceptualization. **A. Baggio:** Writing – review & editing, Writing – original draft, Visualization, Investigation, Formal analysis, Conceptualization. **M. Salvo:** Writing – review & editing, Supervision, Formal analysis, Conceptualization. **F. Smeacetto:** Writing – review & editing, Supervision, Conceptualization.

Declaration of competing interest

The authors declare that they have no known competing financial interests or personal relationships that could have appeared to influence the work reported in this paper.

Acknowledgments

This research was funded by the European Union's Horizon 2020 research and innovation program under grant agreement No. 963599—SOLSTICE, Sodium-Zinc molten salt batteries for low-cost stationary storage.

References

[1] D.R. Sadoway, Electrochemical pathways towards sustainable energy, in: A. Lazou, K. Daehn, C. Fleuriault, M. Gökelma, E. Olivetti, C. Meskers (Eds.), REWAS 2022: Developing Tomorrow's Technical Cycles (Volume I), Springer International Publishing, Cham, 2022, pp. 7–9.

[2] O.E. Godinez-Brizuela, C. Duczek, N. Weber, W. Nash, M. Sarma, K.E. Einarsrud, A continuous multiphase model for liquid metal batteries, J. Energy Storage 73 (2023) 109147, https://doi.org/10.1016/j.est.2023.109147.

[3] H. Kim, D.A. Boysen, J.M. Newhouse, B.L. Spatocco, B. Chung, P.J. Burke, D. J. Bradwell, K. Jiang, A.A. Tomaszowska, K. Wang, W. Wei, L.A. Ortiz, S.A. Barriga, S.M. Poizeau, D.R. Sadoway, Liquid metal batteries: past, present, and future, Chem. Rev. 113 (2013) 2075–2099, https://doi.org/10.1021/cr300205k.

[4] G. De With, P.J. Vrugt, A.J.C. Van De Ven, Sodium corrosion resistance of translucent alumina: effect of additives and sintering conditions, J. Mater. Sci. 20 (1985) 1215–1221, https://doi.org/10.1007/BF01026317.

[5] G. Gunnarsson, B. Johannesson, Corrosion of sodium β″- alumina membranes in molten sodium hydroxide, J. Am. Ceram. Soc. 94 (2011) 988–990, https://doi.org/10.1111/j.1551-2916.2011.04418.x.

[6] J.-L. Courouau, M.-C. Steil, J. Fouletier, F. Rouillard, V. Lorentz, P. Bonnaillie, A. Muccioli, J. Unger, S. Tricoit, M. Tabarant, Single crystal and sintered alumina corrosion in liquid sodium, Oxid Met 87 (2017) 789–800, https://doi.org/10.1007/s11085-017-9743-3.

[7] T. Nagaoka, N. Kondo, Others, hot corrosion of Al2O3 and SiC ceramics by KCl–NaCl molten salt, J. Ceram. Soc. Jpn. 123 (2015) 685–689.

[8] A. Baggio, F. D'Isanto, F. Valenza, S. Gambaro, V. Casalegno, M. Salvo, F. Smeacetto, The joining of alumina to hastelloy by a TiZrCuNi filler metal: wettability and interfacial reactivity, Materials 16 (2023) 1976, https://doi.org/10.3390/ma16051976.

[9] O.S. Kjos, Z. Wang, K.-R. Molvik, S. Rørvik, C.K.W. Solem, C. Sommerseth, Sodium resistance of ceramic and glass materials—Na thermo-gravimetric analysis and liquid Na exposure test, in: TMS 2025 154th Annual Meeting & Exhibition Supplemental Proceedings, Springer Nature Switzerland, Cham, 2025, pp. 1198–1210.

[10] K.M. Hafez, M.H. El-Sayed, M. Naka, Joining of alumina ceramics to metals, Sci. Technol. Weld. Join. 10 (2005) 125–130, https://doi.org/10.1179/174329305X19312.

[11] M.R. Rijnders, S.D. Peteves, Joining of alumina using a V-Active filler metal, Scr. Mater. 41 (1999) 1137–1146, https://doi.org/10.1016/S1359-6462(99)00273-0.

[12] I. Foroutan, R.S. Mamoory, N. Hosseinabadi, Alumina–copper joining by the sintered metal powder process, Ceram. Int. 36 (2010) 741–747, https://doi.org/10.1016/j.ceramint.2009.10.016.

[13] S. Simões, Recent progress in the joining of titanium alloys to ceramics, Metals 8 (2018), https://doi.org/10.3390/met8110876.

[14] G. Elssner, G. Petzow, Metal/ceramic joining, ISIJ Int. 30 (1990) 1011–1032.

[15] Y. Zhang, D. Feng, Z. He, X. Chen, Progress in joining ceramics to metals, J. Iron Steel Res. Int. 13 (2006) 1–5, https://doi.org/10.1016/S1006-706X(06)60032-0.

[16] M.B. Uday, M.N. Ahmad-Fauzi, Alias Mohd Noor, Srithar Rajoo, in: Current Issues and Problems in the Joining of Ceramic to Metal, Joining Technologies, IntechOpen, London, 2016. https://doi.org/10.5772/64524.

[17] M. Salvo, V. Casalegno, S. Rizzo, F. Smeacetto, A. Ventrella, M. Ferraris, Glasses and glass-ceramics as brazing materials for high-temperature applications, in: Advances in Brazing, Elsevier, 2013, pp. 525–544, https://doi.org/10.1533/9780857096500.3.525.

[18] M. Ferraris, V. Casalegno, F. Smeacetto, M. Salvo, Glass as a joining material for ceramic matrix composites: 25 years of research at Politecnico di Torino, Int. J. Appl. Glass Sci. 11 (2020) 569–576, https://doi.org/10.1111/ijag.15032.

[19] C. Malinverni, M. Salvo, A. De Zanet, F. D'Isanto, F. Smeacetto, P. Bertrand, G. Puchas, S. Schafföner, V. Casalegno, Glass-ceramics for joining oxide-based ceramic matrix composites (Al2O3f/Al2O3-ZrO2) operating under direct flame exposure, J. Eur. Ceram. Soc. 43 (2023) 3621–3629, https://doi.org/10.1016/j.jeurceramsoc.2023.02.019.

[20] S. Song, Z. Wen, Y. Liu, Development and characterizations of Bi2O3-containing glass–ceramic sealants for sodium sulfur battery, J. Non-Cryst. Solids 375 (2013) 25–30, https://doi.org/10.1016/j.jnoncrysol.2013.05.010.

[21] M. Herrmann, W. Lippmann, A. Hurtado, High-temperature stability of laser-joined silicon carbide components, J. Nucl. Mater. 443 (2013) 458–466, https://doi.org/10.1016/j.jnucmat.2013.07.067.

[22] M. Ferraris, S.D. la Pierre, Y. Akram, C. Steinborn, G. Puchas, W. Krenkel, High temperature creep behaviour of glass-ceramic joined Nextel 610^{TM}/Al2O3-ZrO2 composites, J. Eur. Ceram. Soc. 42 (2022) 5029–5034, https://doi.org/10.1016/j.jeurceramsoc.2022.04.052.

[23] L. Peng, Q. Zhu, The development of thermally stable sealing glass in the BaO-B2O3-SiO2 system for planar SOFC applications, J. Fuel Cell Sci. Technol. 5 (2008) 8–11, https://doi.org/10.1115/1.2930768.

[24] H. Javed, E. Zanchi, F. D'Isanto, C. Bert, D. Ferrero, M. Santarelli, F. Smeacetto, Novel SrO-Containing glass-ceramic sealants for solid oxide electrolysis cells (SOEC): their design and characterization under relevant conditions, Materials 15 (2022) 1–18, https://doi.org/10.3390/ma15175805.

[25] F. D'Isanto, F. Smeacetto, H.-P. Martin, R. Sedlák, M. Lisnichuk, A. Chrysanthou, M. Salvo, Development and characterisation of a Y2Ti2O7-based glass-ceramic as a potential oxidation protective coating for titanium suboxide (TiOx), Ceram. Int. 47 (2021) 19774–19783, https://doi.org/10.1016/j.ceramint.2021.03.316.

[26] F. D'Isanto, M. Salvo, S. Molin, D. Koszelow, H. Javed, S. Akram, A. Chrysanthou, F. Smeacetto, Glass-ceramic joining of Fe22Cr porous alloy to Crofer22APU: interfacial issues and mechanical properties, Ceram. Int. 48 (2022) 28519–28527, https://doi.org/10.1016/j.ceramint.2022.06.166.

[27] F. Smeacetto, M. Radaelli, M. Salvo, D. Di Modugno, A.G. Sabato, V. Casalegno, M. Broglia, M. Ferraris, Glass-ceramic joining material for sodium-based battery, Ceram. Int. 43 (2017) 8329–8333, https://doi.org/10.1016/j.ceramint.2017.03.170.

[28] D.-S. Park, C. Park, L. Navias, Sodium Resistant Sealing Glasses, 1981.

[29] M.W. Breiter, B.S. Dunn, L. Navias, D. Park, Sodium resistant sealing glasses and sodium-sulfur cells sealed with said glasses 14 (1982) 10–13.

[30] V. Manthina, G. Song, P. Singh, M.K. Mahapatra, Silica-free sealing glass for sodium-beta alumina battery, Int. J. Appl. Ceram. Technol. 16 (2019) 887–895, https://doi.org/10.1111/ijac.13093.

[31] A.J. Burggraaf, H.C. Van Velzen, Glasses resistant to sodium vapor at temperatures to 700°C, J. Am. Ceram. Soc. 52 (1969) 238–242, https://doi.org/10.1111/j.1151-2916.1969.tb09174.x.

[32] S. Kumar, D.-S. Park, Sealing Glass Composition and Article, 2015, p. 2.

[33] R. Benato, N. Cosciani, G. Crugnola, S. Dambone Sessa, G. Lodi, C. Parmeggiani, M. Todeschini, Sodium nickel chloride battery technology for large-scale stationary storage in the high voltage network, J. Power Sources 293 (2015) 127–136, https://doi.org/10.1016/j.jpowsour.2015.05.037.

[34] F. D'Isanto, A. Baggio, M. Salvo, D. Basso, D. Gaia, F. Smeacetto, Glass-based sealants for joining α to β''-Al2O3 in Na–Zn batteries, Ceram. Int. 50 (2024) 14542–14549, https://doi.org/10.1016/j.ceramint.2024.01.367.

[35] A. Baggio, D. Dalmazzo, F. D'Isanto, E. Santagata, D. Basso, D. Gaia, M. Salvo, F. Smeacetto, Optimizing rheological behavior of glass-based sealant inks for robocasting deposition: a design of experiment approach, Mater. Des. 251 (2025) 113678, https://doi.org/10.1016/j.matdes.2025.113678.

[36] US9708212B2, Sodium-Resistant Joining Glass and the Use Thereof, (n.d.).

[37] S. Li, K. Hu, W. Hui, Y. Cai, Y. Zhang, Shear strength and interfacial characterization of borosilicate glass-to-metal seals, J. Alloys Compd. 827 (2020) 154275, https://doi.org/10.1016/j.jallcom.2020.154275.

[38] I.W. Donald, Interfacial reactions and their influence on the lifetime behaviour of glass-ceramic-to-metal seals and coatings, in: L.G. Mallinson (Ed.), Ageing Studies and Lifetime Extension of Materials, Springer US, Boston, MA, 2001, pp. 653–666, https://doi.org/10.1007/978-1-4615-1215-8_72.

[39] T.-S. Chern, H.-L. Tsai, Wetting and sealing of interface between 7056 glass and kovar alloy, Mater. Chem. Phys. 104 (2007) 472–478, https://doi.org/10.1016/j.matchemphys.2007.04.012.

[40] A. Zanchetta, P. Lortholary, P. Lefort, Ceramic to metal sealings: interfacial reactions mechanism in a porcelain-kovar junction, J. Alloys Compd. 228 (1995) 86–95, https://doi.org/10.1016/0925-8388(95)01656-2.

[41] C. Kuo, P. Cheng, C. Chou, Matched glass-to-kovar seals in N2 and Ar atmospheres, Int. J. Min. Met. Mater. 20 (2013) 874–882, https://doi.org/10.1007/s12613-013-0809-1.

[42] Z. Shi, D. Shi, B. Gao, J. Xu, X. Hu, Z. Wang, Oxidation of Fe-Ni alloys in air at 700°C, 800°C and 950°C, High Temp. Mater. Process. 31 (2012), https://doi.org/10.1515/htmp.2011.147.

[43] D. Zhang, X. Du, Y. Song, H. Sun, Y. Zheng, Z. Sun, Y. She, B. Wang, Oxidation mechanism and microstructure evolution of invar alloy with high temperature annealing process, J. Mater. Res. Technol. 32 (2024) 185–195, https://doi.org/10.1016/j.jmrt.2024.07.150.

[44] J. Zygmuntowicz, M. Piatek, A. Miazga, K. Konopka, W. Kaszuwara, Dilatrometric sintering study and characterization of Alumina-nickel composites, processing and application of, Ceramics 12 (2018) 111–117, https://doi.org/10.2298/pac1802111z.

[45] https://www.schott.com/en-gb/products/sealing-and-solder-glass-p1000291/downloads (accessed 12 November 2025), (n.d.).

[46] D14 Committee, Test method for strength properties of adhesive bonds in shear by compression loading, (n.d.). https://doi.org/10.1520/D0905-08R21.

[47] M. Ferraris, M. Salvo, V. Casalegno, S. De La Pierre, L. Goglio, A. Benelli, Torsion test vs. other methods to obtain the shear strength of elastic-plastic adhesives, Appl. Sci. 12 (2022), https://doi.org/10.3390/app12073284.

[48] L.Z. Mohamed, S.S. Abd ElMoamen, F.S. Ahmed, Comparative study of oxidation behavior of Fe–35Ni–22Cr and Fe–17Ni–18Cr alloys in dry air, Chem. Pap. 79 (2025) 7595–7615, https://doi.org/10.1007/s11696-025-04274-3.

[49] A. Sahoo, V.R.R. Medicherla, Fe-Ni invar alloys: a review, Mater. Today Proc. 43 (2021) 2242–2244, https://doi.org/10.1016/j.matpr.2020.12.527.

[50] M.J. Pascual, A. Durán, M.O. Prado, A new method for determining fixed viscosity points of glasses, Phys. Chem. Glasses 46 (2005) 512–520.

[51] H. Deters, H. Eckert, Characterization of the glass-to-vitroceramic transition in yttrium aluminum borate laser glasses using solid state NMR, Solid State Nucl. Magn. Reson. 41 (2012) 48–59, https://doi.org/10.1016/j.ssnmr.2011.11.008.

[52] https://www.hightempmetals.com/techdata/hitempInvar42data.php, (n.d.).

[53] M. Allix, L. Cormier, Crystallization and glass-ceramics, in: J.D. Musgraves, J. Hu, L. Calvez (Eds.), Springer Handbook of Glass, Springer International Publishing, Cham, 2019, pp. 113–167, https://doi.org/10.1007/978-3-319-93728-1_4.

[54] M. Micoulaut, Glass transition temperature variation as a probe for network connectivity, in: M.F. Thorpe, J.C. Phillips (Eds.), Phase Transitions and Self-Organization in Electronic and Molecular Networks, Springer US, Boston, MA, 2001, pp. 143–160, https://doi.org/10.1007/0-306-47113-2_10.

[55] M. Fisch, T. Armbruster, Thermal expansion of aluminoborates, Minerals as Advanced Materials II (2012) 255–268, https://doi.org/10.1007/978-3-642-20018-2_25.